PCCP

PAPER

Cite this: *Phys. Chem. Chem. Phys.*, 2025, **27**, 11879

Axial coordination engineering for single-atom catalysts in bifunctional oxidation of NO and mercury†

Jianghao Cai,[ab] Tongao Yao,[ab] Haoqi Tian,[ab] Xiaotian Tang,[ab] Yutong Jiang,[ab] Ruiyang Shi,[ab] Binghui Zhou,[ab] Zhengyang Gao[ab] and Weijie Yang *[ab]

Coal-fired power plants are major emitters of nitrogen oxides (NO) and elemental mercury (Hg^0), both of which pose significant environmental and health risks. While wet flue gas desulfurization (WFGD) and electrostatic precipitators (ESP) are effective in removing oxidized mercury (Hg^{2+}) and particulate-bound mercury (Hg^P), capturing volatile Hg^0 remains a significant challenge. Catalytic oxidation is a promising approach to convert NO and Hg^0 into their more easily captured oxidized forms (NO_2 and Hg^{2+}), highlighting the need for highly efficient catalysts. In this study, graphene-supported iron single-atom catalysts (Fe SACs) with various axial ligands were systematically investigated using density functional theory (DFT). Adsorption energies of O_2 and NO, along with energy barriers for key oxidation steps, were calculated to evaluate catalytic performance. Among the ten Fe_1N_4–X catalysts examined, Fe_1N_4–Br exhibited the lowest reaction energy barriers, while Fe_1N_4–H_2O showed the highest turnover frequency (TOF) for both NO and Hg^0 oxidation under simulated flue gas conditions. These results demonstrate the importance of axial ligand coordination in tuning catalytic activity. This work offers theoretical insights for the rational design of high-performance SACs for pollutant control in coal-fired flue gas treatment systems.

Received 9th May 2025,
Accepted 19th May 2025

DOI: 10.1039/d5cp01745a

rsc.li/pccp

1. Introduction

Coal-fired power plants release flue gases containing hazardous pollutants such as nitrogen oxides (primarily NO) and elemental mercury (Hg^0), which are known to cause environmental harm and serious health risks, particularly respiratory illnesses.[1–3] Mercury in flue gas typically exists in three forms: elemental mercury (Hg^0), oxidized mercury (Hg^{2+}), and particle-bound mercury (Hg^P). While wet flue gas desulfurization (WFGD) and electrostatic precipitators (ESP) are effective at removing Hg^{2+} and Hg^P, the removal of Hg^0 remains challenging due to its low solubility and high volatility. Therefore, developing a cost-effective and efficient approach for the simultaneous removal of NO and Hg^0 is critical. Oxidizing NO and Hg^0 into NO_2 and Hg^{2+} facilitates their removal *via* absorption in alkaline solutions, highlighting the importance of designing catalysts with high activity to enhance catalytic oxidation processes targeting these pollutants.[4]

Graphene-supported single-atom catalysts (SACs) have emerged as promising materials due to their exceptional catalytic performance across various applications, including electrocatalysis, photocatalysis, and thermal catalysis.[5–8] In thermal oxidation reactions, SACs demonstrate excellent reactivity and selectivity. For instance, Chen *et al.*[9] employed transition state analysis and microkinetic modeling to reveal that $Ni_1N_1C_2$ exhibits outstanding catalytic activity for CO oxidation. Yang *et al.*[10] conducted systematic studies on graphene-based SACs for O_2-mediated Hg^0 oxidation, offering new perspectives on mercury pollution control in coal-fired power systems. Liu *et al.*[11] showed that Pd atoms anchored on graphene can efficiently catalyze low-temperature CO oxidation *via* the Langmuir–Hinshelwood (LH) mechanism. Their subsequent theoretical investigations confirmed that Fe_1N_2 structures also possess high CO oxidation activity under the same mechanism.[12] Dong *et al.*[13] explored how varying nitrogen coordination affects the adsorption of NO and O_2 on Co-based SACs, identifying Co_1N_3 as a promising NO oxidation catalyst. Yang *et al.*[14] investigated carbon-supported iron SACs and demonstrated their potential in catalyzing NO oxidation. Furthermore, Yang *et al.*[15] experimentally verified that Fe_1N_4 shows excellent low-temperature catalytic activity for the simultaneous oxidation

---

[a] *Department of Power Engineering, School of Energy, Power and Mechanical Engineering, North China Electric Power University, Baoding, 071003, China. E-mail: yangwj@ncepu.edu.cn*

[b] *Hebei Key Laboratory of Low Carbon and High Efficiency Power Generation Technology, North China Electric Power University, Baoding, 071003, Hebei, China*

† Electronic supplementary information (ESI) available. See DOI: **https://doi.org/10.1039/d5cp01745a**

of NO and Hg^0. Although SACs have proven highly effective for oxidizing these pollutants both theoretically and experimentally, strategies for tuning their catalytic activity remain insufficiently developed.

Recent studies have demonstrated that modifying the axial coordination environment of graphene-based single-atom catalysts (SACs) by introducing functional groups such as H, H_2O, CN, O_2, NH_3, and NO_2,[16–18] as well as halogen elements like F, Cl, Br, and I,[19–21] can significantly enhance their catalytic activity. For instance, Tang *et al.*[22] optimized the coordination structure of Co-based SACs by co-doping with B and N, achieving remarkable catalytic performance for NO and CO oxidation. Similarly, Li *et al.*[23] showed that co-doping N and O into Mn-based SACs influences the adsorption energy of elemental mercury (Hg^0), depending on the number of N and O atoms surrounding the metal center. Yang *et al.*[6] found that incorporating p-block elements into Fe-based SACs effectively tunes the adsorption free energy of oxygen evolution reaction (OER) intermediates, thereby modulating OER catalytic activity. Such p-block element doping strategies are thus valuable for tailoring coordination environments and enhancing the adsorption behavior of reactant gases. Nevertheless, reducing the energy barriers for NO and Hg^0 oxidation by fine-tuning the active site composition remains a major challenge.

Motivated by this background, we systematically investigated the adsorption behaviors of key intermediates (O_2, O, and NO) on Fe-based SACs with varied coordination environments and aimed to identify high-performance Co-based SACs for the dual oxidation of NO and Hg^0. To this end, we constructed ten Co-based SACs with distinct axial coordination configurations and conducted spin-polarized density functional theory (DFT-D3) calculations incorporating van der Waals corrections. First, ten Fe SACs with different ligand environments were modeled. Then, their adsorption energies toward O and O_2 were calculated and analyzed. Reaction pathway computations were further employed to determine the catalytic energy barriers for NO and Hg^0 oxidation, revealing that Fe_1N_4–Br exhibited the highest catalytic activity. Moreover, microkinetic modeling indicated that Fe_1N_4–H_2O delivered the best overall performance among all ten catalysts. This study offers a theoretical framework for rational catalyst design and highlights the importance of local coordination environment modulation in developing high-efficiency SACs for NO and Hg^0 oxidation.

2. Computational details

2.1. Methods

In this work, density functional theory (DFT) calculations were performed using the Vienna Ab initio simulation package (VASP 5.4.4).[24,25] The interactions between atomic cores and valence electrons were described using the projector augmented wave (PAW) method, while the Perdew–Burke–Ernzerhof (PBE) functional was adopted to account for exchange–correlation effects.[26] Spin polarization was incorporated to obtain accurate ground-state electronic structures. To ensure a realistic description of the gas and surface interactions, both dipole corrections and Grimme's DFT-D3 dispersion corrections were employed.[27] A $5 \times \sqrt{3} \times 1$ graphene supercell ($12.33 \times 12.88 \times 20.00$ Å) was constructed as the catalyst substrate, with a vacuum gap of 20.00 Å introduced along the *z*-direction to eliminate interactions between periodic images. The plane-wave cutoff energy was set at 450 eV for all computations. Geometry optimization and frequency analyses were performed using a $2 \times 2 \times 1$ Monkhorst–Pack *k*-point mesh, with a force convergence threshold of 0.02 eV Å^{-1}. A denser *k*-point grid of $4 \times 4 \times 1$ was used for self-consistent field (SCF) calculations, with an energy convergence criterion of 10^{-5} eV. In this work, we focused on adsorption energy and energy barrier analysis as the main descriptors of catalytic activity. Charge density or Bader charge analysis was not included, but will be considered in future studies.

2.2. Energy calculations

To precisely identify the transition state (TS) structures and associated energy barriers for NO and Hg^0 oxidation, a combination of the climbing-image nudged elastic band (CI-NEB) method[28,29] and the improved dimer method (IDM)[30] was utilized. The CI-NEB approach was first employed to estimate the initial TS geometry, using a force threshold of 0.5 eV Å^{-1}. This configuration was subsequently refined with the IDM method, applying a tighter convergence standard of 0.05 eV Å^{-1}. To verify the validity of each transition state, we ensured that the optimized TS structure exhibited a single imaginary frequency corresponding to the appropriate vibrational mode, using a finite displacement of ±0.02 Å for frequency analysis.

The adsorption energies were calculated by the following equation:

$$E_{\text{ads}} = E_{\text{sur+gas}} - E_{\text{sur}} - E_{\text{gas}} \tag{1}$$

where $E_{\text{sur+gas}}$, E_{sur}, and E_{gas} are the electronic energies of the catalyst with adsorbate, catalyst, and gas species, respectively. It is worth noting that when calculating the adsorption energy of the O atom, the energy of the O atom is taken as half the energy of the O_2 molecule.

The energy barrier (E_{b}) was obtained by the following equations, respectively:

$$E_{\text{b}} = E_{\text{TS}} - E_{\text{IS}} \tag{2}$$

where E_{IS}, and E_{TS} are the energies of the initial and transition states, respectively.

2.3. Microkinetic modelling methods

In conclusion, we applied a microkinetic modeling approach grounded in Sabatier analysis[31] to estimate the theoretical upper limit of the reaction rates for NO and Hg^0 oxidation. The Sabatier rate refers to the idealized scenario in which each elementary step proceeds under optimal conditions, offering a useful benchmark for assessing the intrinsic catalytic performance of a surface. This approach aligns with methodologies previously reported for oxidation reaction modeling.[32,33]

The NO oxidation pathway can be decomposed into the following four elementary steps:

$$O_2 + * \rightarrow O_2^* \tag{R1}$$

$$O_2^* + NO \rightarrow NO_2 + O^* \tag{R2}$$

$$O^* + NO \rightarrow NO_2^* \tag{R3}$$

$$NO_2^* \rightarrow NO_2 + * \tag{R4}$$

where (R1) is assumed to be in equilibrium. The forward rate constants of the remaining steps are given by:

$$k_i = \nu_i \exp\left(-\frac{\Delta G_{\mathrm{a}i}}{KT}\right) = \nu_i \exp\left[-\frac{E_{\mathrm{a}i} - T\Delta S_{\mathrm{a}i}}{KT}\right] \tag{3}$$

where ν_i is the prefactor, E_{ai} is the activation energy, and ΔS_{ai} is the entropy difference between the transition state and the initial state, k is the Boltzmann constant, and T is the temperature. ν_i is estimated by kT/h, where h is the Planck's constant.

Assuming (R1) is in equilibrium, this gives:

$$\theta_{O_2} = \frac{1}{1 + K_i p(O_2)} \tag{4}$$

where K_i is the equilibrium constant of (R1), $p(O_2)$ is the partial pressure of O_2. K_i was calculated by:

$$K_i = \exp\left(-\frac{G_i}{kT}\right) \tag{5}$$

where G_1 is the free energy of (R1). The Sabatier rate $\left(r_i^{S_{\max}} = \theta_i k_i\right)$ of the overall reaction (r_S) was estimated by the minimum reaction rate among (R2)–(R4) as a function of O adsorption energy:

$$r_{\mathrm{s}} = \min[r_2^{S_{\max}}, r_3^{S_{\max}}, r_4^{S_{\max}}] \tag{6}$$

Similarly, the Hg^0 oxidation reaction can also be analyzed in the following four elementary steps according to the above analysis method of NO oxidation:

$$O_2 + * \rightarrow O_2^* \tag{R5}$$

$$O_2^* + Hg \rightarrow HgO^* \tag{R6}$$

$$HgO^* + Hg \rightarrow (HgO)_2^* \tag{R7}$$

$$(HgO)_2^* \rightarrow (HgO)_2 + * \tag{R8}$$

3. Results and discussion

3.1. Catalyst model

Two-dimensional single-atom catalysts (SACs) supported on graphene are widely utilized as model systems for carbon-based SACs due to their well-defined structure and experimental feasibility. In this study, graphene was employed as the substrate, and a double-vacancy defect was introduced to create a stable anchoring site for isolated metal atoms. Iron (Fe) was selected as the active metal due to its abundance and cost-effectiveness, and was embedded into the vacancy site. To optimize the coordination environment, four adjacent carbon atoms were replaced with nitrogen atoms, resulting in a classic Fe_1N_4 coordination structure.

To further modulate the physicochemical properties of the catalyst, various axial ligands, comprising functional groups (H, H_2O, CN, O_2, NH_3, NO_2) and halogen elements (F, Cl, Br, I),

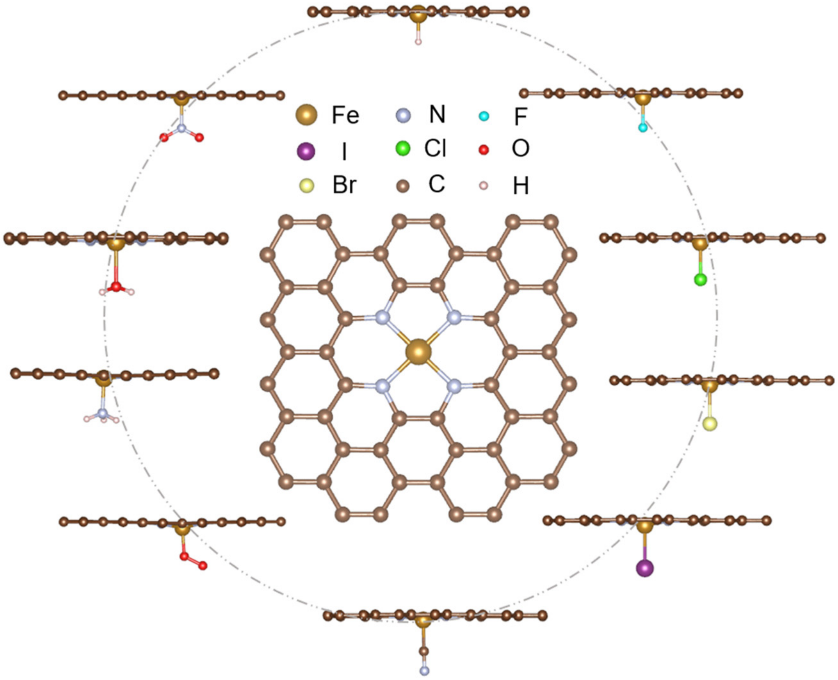

Fig. 1 10 different axial coordination environments of Fe_1N_4–X single atom iron catalyst configurations.

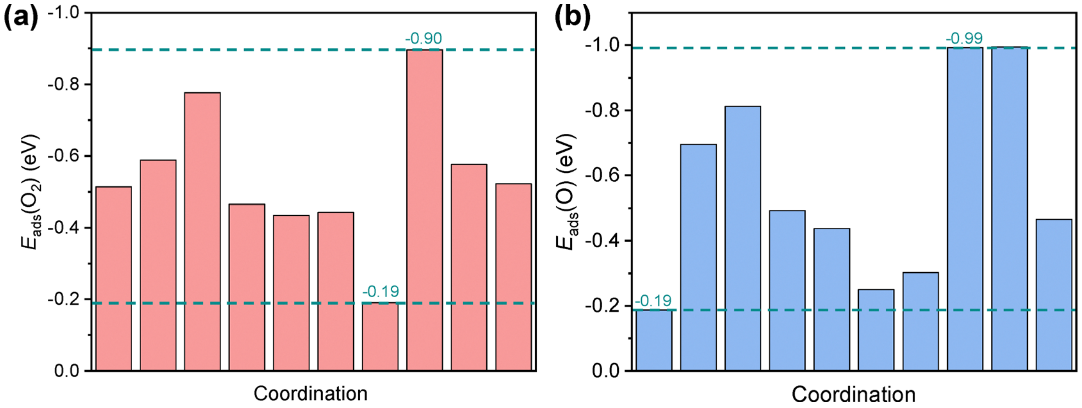

Fig. 2 (a) Adsorption energy of 10 different axial coordination configurations of Fe_1N_4–X single atom iron catalysts for O_2 (b) adsorption energy of 10 different axial coordination configurations of Fe_1N_4–X single atom iron catalysts for O.

were introduced beneath the Fe center. This axial coordination strategy enables fine-tuning of both the geometric and electronic characteristics of the active site. As a result, a series of ten Fe_1N_4–X catalysts with distinct axial configurations were systematically designed, where X represents a specific ligand or dopant. In each structure, a single axial ligand was positioned on one side of the Fe center, leaving the opposite side exposed to accommodate gas-phase reactants. This asymmetric configuration reflects typical coordination environments in experimentally studied Fe-based SACs. The doping sites and corresponding structural models are illustrated in Fig. 1. These tailored structures are expected to significantly influence catalytic activity by altering the local electronic and geometric environment around the Fe center, thereby offering insights into the structure–activity relationships in single-atom catalysis.

3.2. Adsorption properties

The adsorption energies of O_2 and atomic O are pivotal for evaluating the catalytic efficiency of single-atom catalysts (SACs) in the oxidation of NO and Hg^0.[34,35] To investigate this aspect, we systematically calculated the adsorption energies of O_2 and O on a series of ten Fe_1N_4–X catalysts. The results are

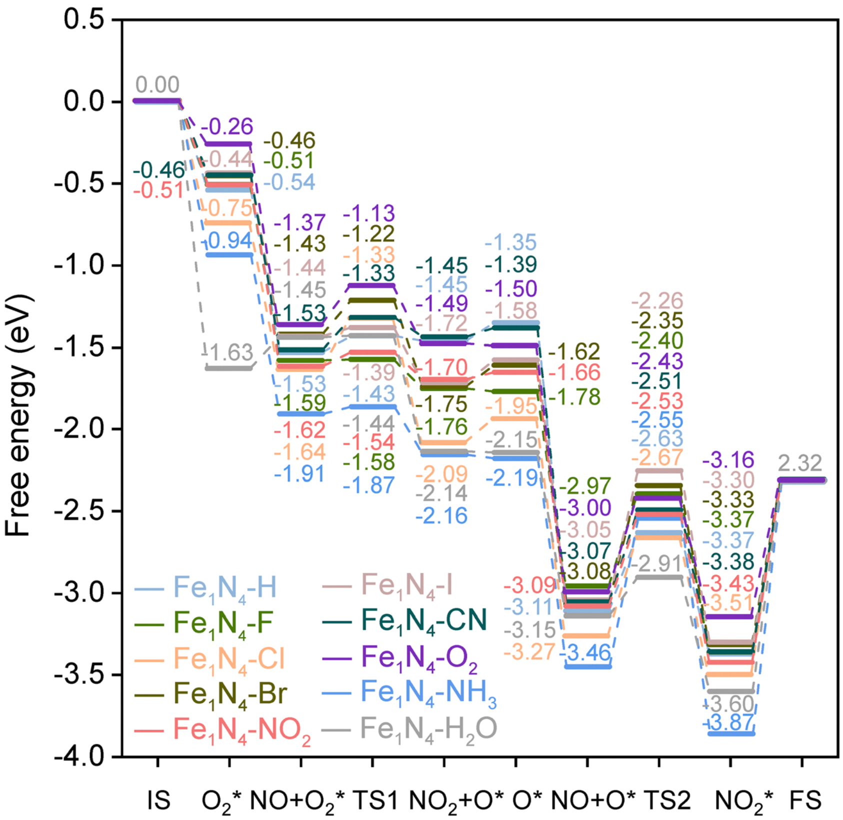

Fig. 3 Energy variation diagram of ten single atom iron axial coordination catalysts for NO oxidation.

illustrated in Fig. 2(a) and (b). Two primary adsorption geometries were identified for the O_2 molecule: the side-on configuration ($E_{ads}(O_{2side})$) and the end-on configuration ($E_{ads}(O_{2end})$). For most of the catalysts, the side-on mode was found to be thermodynamically more stable, indicating a stronger interaction between the Fe center and the O_2 molecule in this arrangement.

As shown in the figures, modifications to the axial ligand environment significantly affect the adsorption strengths of both O_2 (ranging from −0.19 to −0.90 eV) and O (from −0.19 to −1.00 eV). These results demonstrate that tuning the local coordination environment is an effective approach to modulate the adsorption behavior of reactive species, thereby enhancing catalytic performance. This insight is valuable for the rational development of efficient SACs for environmental applications. Note that a negative adsorption energy indicates an exothermic adsorption process, which corresponds to favorable interaction between the adsorbate and the catalyst surface.

3.3. Reaction pathway analysis

To assess the catalytic performance of the ten axially coordinated single-atom iron catalysts, the oxidation pathways for NO and Hg^0 were comprehensively examined using energy profile calculations.[10] The reaction energy diagram for NO oxidation is presented in Fig. 3. Among the catalysts, Fe_1N_4–Br demonstrates superior activity, evidenced by its lower energy barrier in the rate-determining step (RDS), indicating efficient catalytic oxidation under relatively mild conditions. In contrast, Fe_1N_4–CN and Fe_1N_4–I show higher energy barriers, implying that these systems may require additional energy input to achieve comparable reactivity. The corresponding energy pathways for Hg^0 oxidation on each catalyst are provided in Fig. S10–S19 (ESI†).

Previous studies suggest that the Eley–Rideal (ER) mechanism is likely the dominant reaction pathway for NO and Hg^0 oxidation.[36–38] Following this mechanistic framework, we computed the detailed oxidation steps and associated energy barriers on the Fe_1N_4–Br catalyst, as depicted in Fig. 4. Given the consistent reaction trends across different catalysts, the reaction profiles and free energy diagrams for the remaining nine systems are summarized in Fig. S1–S9 (ESI†).

As illustrated in Fig. 4(a), the NO oxidation pathway begins with the pre-adsorption of O_2 at the Fe active site. Subsequently, an incoming NO molecule reacts with the adsorbed O_2, forming the first NO_2 molecule while overcoming a low energy barrier of 0.21 eV. A second NO molecule then interacts with the remaining O atom to yield another NO_2 molecule, requiring a barrier of

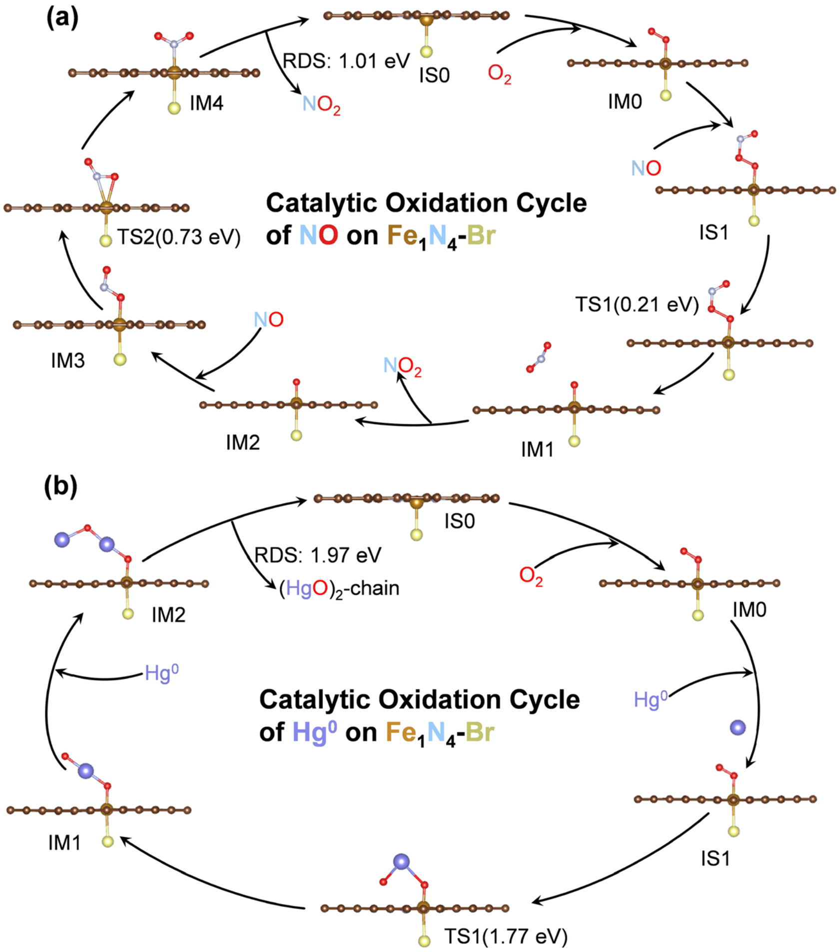

Fig. 4 (a) Catalytic oxidation cycle of NO and (b) catalytic oxidation cycle of Hg^0 on Fe_1N_4–Br.

Table 1 The four catalysts RDS and TOF/s of oxidation NO and Hg^0, respectively. The temperature is 400 K and the oxygen pressure is 0.05 bar

	RDS		TOF/s	
SACs	Oxidation NO (eV)	Oxidation Hg^0 (eV)	Oxidation NO	Oxidation Hg^0
Fe_1N_4–H_2O	1.29	2.37	1.14×10^{8}	4.72×10^{-14}
Fe_1N_4–NH_3	1.55	2.46	2.85×10	4.23×10^{-15}
Fe_1N_4–Br	1.01	1.98	5.29×10^{3}	2.82×10^{-16}
Fe_1N_4–Cl	1.19	2.24	2.30×10^{5}	2.64×10^{-16}
Fe_1N_4–F	1.05	2.15	5.49×10^{5}	1.44×10^{-19}
Fe_1N_4–NO_2	1.11	2.05	7.08×10^{5}	6.00×10^{-20}
Fe_1N_4–H	1.05	2.01	1.31×10^{6}	6.46×10^{-22}
Fe_1N_4–CN	1.06	1.95	9.11×10^{3}	5.35×10^{-22}
Fe_1N_4–I	0.98	1.95	9.28×10^{2}	1.06×10^{-23}
Fe_1N_4–O_2	0.84	1.60	1.91	1.25×10^{-24}

0.73 eV. Finally, the desorption of the second NO_2 completes the catalytic cycle, with an associated barrier of 0.98 eV. This desorption step is identified as the rate-determining step (RDS) for NO oxidation on Fe_1N_4–Br, resulting in an overall energy barrier of 1.01 eV.

In the case of Hg^0 oxidation (Fig. 4(b)), the process is initiated by the interaction of a Hg atom with pre-adsorbed O_2, forming a transient O–Hg–O structure, which requires overcoming a barrier of 1.77 eV. A second Hg atom is then adsorbed to generate the final oxidation product, a $(HgO)_2$ chain. The desorption of this chain from the catalyst surface, with an energy barrier of 1.97 eV, marks the completion of the reaction. Thus, $(HgO)_2$ desorption is the RDS in the Hg^0 oxidation pathway.

Table 1 summarizes the rate-determining steps across all ten catalysts. Among them, Fe_1N_4–Br exhibits the lowest RDS energy barriers for both NO and Hg^0 oxidation, highlighting its potential as a highly effective bifunctional catalyst for simultaneous removal of NO and elemental mercury from flue gas streams.

3.4. Microkinetic modelling

To evaluate the catalytic performance of the ten axially coordinated Fe-based single-atom catalysts under realistic flue gas conditions, microkinetic modeling was conducted using

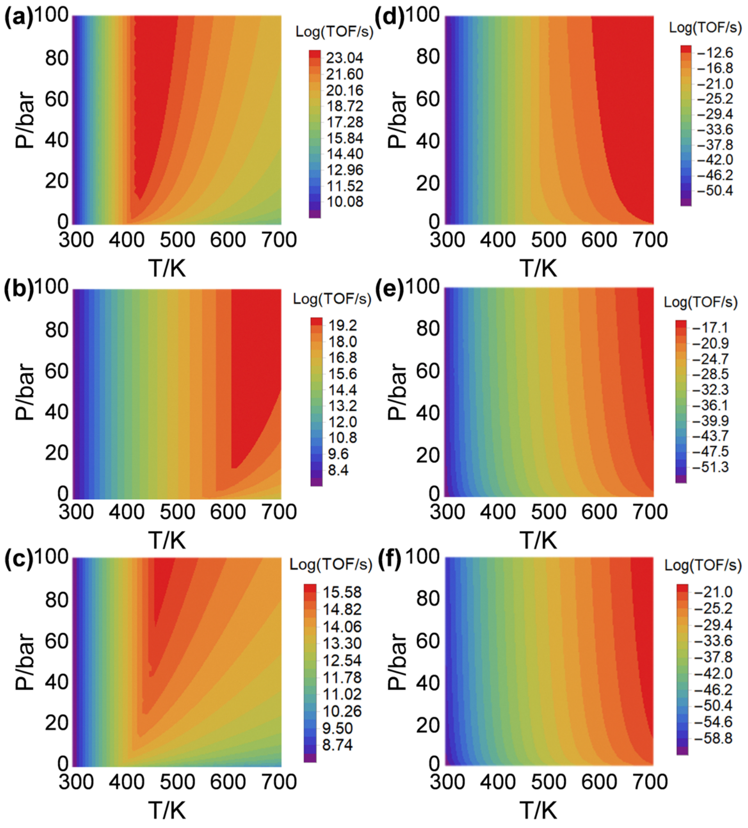

Fig. 5 Microkinetic modeling analyses of the overall flue gas pressure and temperature functions in the process of catalytic oxidation NO by (a, d) Fe_1N_4–H_2O, (b, e) Fe_1N_4–F and (c, f) Fe_1N_4–CN.

kinetic parameters and methodologies. Temperature (T) and pressure (P) were employed as primary variables, with the logarithm of turnover frequency [log(TOF)] serving as the key performance descriptor. As shown in Fig. 5, Fe_1N_4–H_2O exhibited the highest catalytic activity for both NO and Hg^0 oxidation around 400 K, which is closely aligned with the typical operational conditions of coal-fired flue gas systems.[39] This result highlights Fe_1N_4–H_2O as a particularly promising candidate for practical environmental applications.

To further quantify catalyst performance under simulated flue gas conditions, specific TOF values were computed for each system. Following established protocols,[39] the reaction environment was set at 400 K and 1 bar total pressure, with molecular oxygen comprising 5% of the gas mixture.[40] Under these conditions (400 K, $P_{O_2} = 0.05$ bar), TOF values for both NO and Hg^0 oxidation were determined. A comparative summary of the maximum, median, and minimum TOF values is presented in Fig. 5, while the complete dataset can be found in Table 1 and Fig. S20–S26 (ESI†). Notably, Fe_1N_4–H_2O consistently achieved the highest TOF values for both reactions, whereas Fe_1N_4–CN showed the lowest catalytic activity. These results reinforce the superior bifunctional catalytic behavior of Fe_1N_4–H_2O under conditions representative of industrial flue gas treatment. These theoretical predictions are in line with recent experimental studies. For example, Yang *et al.*[15] demonstrated that Fe-based SACs with axial coordination exhibit strong activity toward simultaneous NO and Hg^0 oxidation. Similarly, Ma *et al.*[41] showed that iron-based single-atom materials are efficient catalysts for oxidative transformations. These reports support the relevance of our theoretical findings to real-world catalytic systems.

4. Conclusion

This study systematically investigated graphene-based Fe single-atom catalysts (SACs) with a variety of axial ligands for the catalytic oxidation of NO and elemental mercury (Hg^0). Reaction pathway analysis revealed that Fe_1N_4–Br exhibits relatively low energy barriers for the rate-determining steps (1.01 eV for NO oxidation and 1.97 eV for Hg^0 oxidation). However, microkinetic simulations under flue gas conditions identified Fe_1N_4–H_2O as the catalyst with the highest turnover frequency (TOF) for both reactions at approximately 400 K.

These results demonstrate that TOF and reaction energy barriers are not simply inversely correlated, but are strongly influenced by the relative energies of reaction intermediates and the overall thermodynamic landscape. This distinction arises because TOF calculations account for the full reaction network, including all elementary steps, intermediate stabilities, and entropic contributions, whereas the RDS reflects only the highest single energy barrier along the pathway. To provide a comprehensive assessment, we evaluated the two metrics separately and ultimately identified Fe_1N_4–H_2O as the most effective bifunctional catalyst due to its superior overall kinetic performance. Overall, this work offers theoretical insight into how axial ligand coordination modulates catalytic performance, providing a useful strategy for the rational design of high-activity SACs for pollutant control in coal-fired flue gas purification systems.

Author contributions

Zhengyang Gao and Weijie Yang conceived and supervised the project. Weijie Yang corrected the writing of the manuscript, guided the manuscript throughout the writing process, and the structure construction of the paper, the relevant theoretical support, and the research subject and ideas of the paper. Jianghao Cai, Tongao Yao and Haoqi Tian wrote the first draft of the thesis, completed the revision of the thesis under the supervisor's guidance, and completed the calculation of the thesis results and graphical plotting work. Xiaotian Tang, Yutong Jiang and Binghui Zhou provided the relevant research data for the thesis. Weijie Yang participated in the revision of the manuscript, verified the thesis, and carefully reviewed the results of each part of the paper. Ruiyang Shi participated in the correction of the manuscript. All authors discussed the results.

Data availability

The data supporting this article have been included as part of the ESI.†

Conflicts of interest

There are no conflicts to declare.

Acknowledgements

This work was funded by the National Natural Science Foundation of China (No. 52006073 and 52176104).

References

1 F. B. Elehinafe, E. A. Aondoakaa, A. F. Akinyemi, O. Agboola and O. B. Okedere, *Heliyon*, 2024, **10**, e32428.
2 G. Wang, J. Deng, Y. Zhang, Q. Zhang, L. Duan, J. Hao and J. Jiang, *Sci. Total Environ.*, 2020, **741**, 140326.
3 B. Thitakamol, A. Veawab and A. Aroonwilas, *Int. J. Greenhouse Gas Control*, 2007, **1**, 318–342.
4 J. Georgin, D. S. P. Franco, Y. Dehmani, P. Nguyen-Tri and N. El Messaoudi, *Sci. Total Environ*, 2024, **947**, 174501.
5 Y. Tang, J. Shi, W. Chen, Y. Li, H. Tian, Y. Cui, Z. Wang, Z. Feng and X. Dai, *Fuel*, 2022, **319**, 123810.
6 W. Yang, J. Ren, H. Zhang, J. Li, C. Wu, I. D. Gates and Z. Gao, *Fuel*, 2021, **302**, 121041.
7 L. Sun, Y. Feng, K. Ma, X. Jiang, Z. Gao, J. Wang, N. Jiang and X. Liu, *Appl. Catal., B*, 2022, **306**, 121106.
8 H.-Y. Zhuo, X. Zhang, J.-X. Liang, Q. Yu, H. Xiao and J. Li, *Chem. Rev.*, 2020, **120**, 12315–12341.

9 T. Chen, Y. Ji, Y.-M. Ding and Y. Li, *Phys. Chem. Chem. Phys.*, 2022, **24**, 29586–29593.

10 W. Yang, L. Li, M. Zhao, H. Huang, X. Ding, C. Wu, I. D. Gates and Z. Gao, *Appl. Surf. Sci.*, 2020, **508**, 145035.

11 X. Liu, M. Xu, L. Wan, H. Zhu, K. Yao, R. Linguerri, G. Chambaud, Y. Han and C. Meng, *ACS Catal.*, 2020, **10**, 3084–3093.

12 M. Liu, C. Liu, S. Gouse Peera and T. Liang, *Chem. Phys.*, 2022, **559**, 111536.

13 J. Dong, Z. Gao, W. Yang, A. Li and X. Ding, *Appl. Surf. Sci.*, 2019, **480**, 779–791.

14 W. Yang, Z. Gao, X. Liu, X. Li, X. Ding and W. Yan, *Catal. Sci. Technol.*, 2018, **8**, 4159–4168.

15 W. Yang, X. Liu, X. Chen, Y. Cao, S. Cui, L. Jiao, C. Wu, C. Chen, D. Fu, I. D. Gates, Z. Gao and H.-L. Jiang, *Adv. Mater.*, 2022, **34**, 2110123.

16 Z. Gao, C. Wang, M. Li, Z. Miao, Y. Liu, K. Guo, Y. Zhang and W. Yang, *Energy Fuels*, 2025, **39**, 4471–4480.

17 L.-H. Xu, W. Liu and K. Liu, *Adv. Funct. Mater.*, 2023, **33**, 2304468.

18 J. Yu, X. Yong, A. Cao and S. Lu, *Acta Phys.-Chim. Sin.*, 2024, **40**, 2307015.

19 X. Chen, Y. Zhang, X. Zhao, H. Yu and H. Zhang, *J. Phys. Chem. C*, 2023, **127**, 14107–14116.

20 Z. Li, R. Wu, S. Xiao, Y. Yang, L. Lai, J. S. Chen and Y. Chen, *Chem. Eng. J.*, 2022, **430**, 132882.

21 J.-X. Peng, W. Yang, Z. Jia, L. Jiao and H.-L. Jiang, *Nano Res.*, 2022, **15**, 10063–10069.

22 Y. Tang, W. Chen, J. Shi, Z. Wang, Y. Cui, D. Teng, Y. Li, Z. Feng and X. Dai, *J. Mater. Chem. A*, 2021, **9**, 15329–15345.

23 J. Li, H. Xu, Y. Liao, Y. Qiu, N. Yan and Z. Qu, *Environ. Sci. Technol.*, 2020, **54**, 5249–5257.

24 G. Kresse and J. Furthmüller, *Comput. Mater. Sci.*, 1996, **6**, 15–50.

25 G. Kresse and D. Joubert, *Phys. Rev. B: Condens. Matter Mater. Phys.*, 1999, **59**, 1758–1775.

26 G. Kresse and J. Furthmüller, *Phys. Rev. B: Condens. Matter Mater. Phys.*, 1996, **54**, 11169–11186.

27 S. Grimme, J. Antony, S. Ehrlich and H. Krieg, *J. Chem. Phys.*, 2010, **132**, 154104.

28 G. Henkelman, B. P. Uberuaga and H. Jónsson, *J. Chem. Phys.*, 2000, **113**, 9901–9904.

29 G. Henkelman and H. Jónsson, *J. Chem. Phys.*, 2000, **113**, 9978–9985.

30 A. Heyden, A. T. Bell and F. J. Keil, *J. Chem. Phys.*, 2005, **123**, 224101.

31 T. Bligaard, J. K. Nørskov, S. Dahl, J. Matthiesen, C. H. Christensen and J. Sehested, *J. Catal.*, 2004, **224**, 206–217.

32 H. Li, A. Cao and J. K. Nørskov, *ACS Catal.*, 2021, **11**, 12052–12057.

33 H. Falsig, B. Hvolbæk, I. S. Kristensen, T. Jiang, T. Bligaard, C. H. Christensen and J. K. Nørskov, *Angew. Chem., Int. Ed.*, 2008, **47**, 4835–4839.

34 S. Liu and S. Huang, *Carbon*, 2017, **115**, 11–17.

35 X. Liu, Z. Gao, H. Huang, G. Yan, T. Huang, C. Chen, W. Yang and X.-L. Ding, *Mol. Catal.*, 2020, **488**, 110901.

36 W. Yang, Y. Feng, X. Chen, C. Wu, F. Wang, Z. Gao, Y. Liu, X. Ding and H. Li, *J. Environ. Chem. Eng.*, 2022, **10**, 108744.

37 C. Si, M. Yang and B. Li, *J. Phys. Chem. C*, 2022, **126**, 18275–18281.

38 W. Yang, X. Chen, Y. Feng, F. Wang, Z. Gao, Y. Liu, X. Ding and H. Li, *Environ. Sci.: Nano*, 2022, **9**, 2041–2050.

39 J. Fu, N. Hu, Z. Yang and L. Wang, *J. Water Proc. Eng.*, 2018, **26**, 100–107.

40 Y. Artanto, J. Jansen, P. Pearson, T. Do, A. Cottrell, E. Meuleman and P. Feron, *Fuel*, 2012, **101**, 264–275.

41 Z. Ma, C. Kuloor, C. Kreyenschulte, S. Bartling, O. Malina, M. Haumann, P. W. Menezes, R. Zbořil, M. Beller and R. V. Jagadeesh, *Angew. Chem., Int. Ed.*, 2024, **63**, e202407859.